

## Warped Disk Galaxies: Statistical Properties from DESI Legacy Imaging Surveys DR8

YIHENG WANG <sup>1,2</sup> HAN QU <sup>1,2</sup> JIAFENG LU <sup>3,4</sup> HUIYUAN WANG <sup>5,2</sup> ENCI WANG <sup>5,2</sup> AND XI KANG <sup>3,4,1</sup>

<sup>1</sup>*Purple Mountain Observatory, Chinese Academy of Sciences, Nanjing 210023, Jiangsu, China*

<sup>2</sup>*School of Astronomy and Space Sciences, University of Science and Technology of China, Hefei, Anhui 230026, China*

<sup>3</sup>*Institute for Astronomy, School of Physics, Zhejiang University, Hangzhou 310058, Zhejiang, China*

<sup>4</sup>*Center for Cosmology and Computational Astrophysics, Zhejiang University, Hangzhou 310058, Zhejiang, China*

<sup>5</sup>*Department of Astronomy, University of Science and Technology of China, Hefei, 230026, China*

### ABSTRACT

Warped structures are often observed in disk galaxies, yet their physical origin is still under investigation. We present a systematic study of warped edge-on disk galaxies based on imaging data from the DESI Legacy Imaging Surveys DR8, with the expectation that this large sample size, enabled by wide-area surveys, will offer new perspectives on the formation of disk warps. Using a deep learning approach, we trained an EfficientNet-B3 convolutional neural network to classify the morphology of edge-on-disk galaxies into warped and non-warped categories. Our model was trained on a curated and visually verified set of labeled galaxy images and applied to a large dataset of over 595,651 edge-on disk galaxies selected from the Galaxy Zoo DESI catalog. Our results provide the largest warp catalog to date, consisting of 23996 warped edge-on disk galaxies, and reveal statistical trends between warp occurrence and galaxy properties. Compared to their non-warped counterparts, these warped disk galaxies tend to have bluer colors, lower stellar masses, higher gas fractions and star-formation rates, smaller Sérsic indices and larger disk sizes. In addition, warped disk galaxies show higher projected number densities of neighboring galaxies than their non-warped counterparts, particularly within  $R_{\text{proj}} \lesssim 50$  kpc, where the local number density is roughly twice as high.

*Keywords:* Galaxy evolution(594) — Disk galaxies(391) — Convolutional neural networks(1938) — Galaxy structure(622)

### 1. INTRODUCTION

Galaxies display diverse structures in their morphology, including spiral arms, stellar bars, central bulges, and tidal substructures. These morphological features serve as both tracers and drivers of galaxy evolution. Bulges influence galaxy evolution by stabilizing the central regions, regulating gas inflows, and often correlating with star formation quenching and black hole growth (e.g., Kormendy & Kennicutt 2004; Bluck et al. 2014; Kormendy & Ho 2013), while bars drive gas from the disk toward the center (Sakamoto et al. 1999), fueling star formation and potentially triggering active galactic nuclei (Shlosman et al. 1989; Sheth et al. 2005), thus

playing a crucial role in secular evolutionary processes. Tidal substructures may indicate past interactions that dynamically reshape galaxy structure (Springel & White 1999; Johnston et al. 1999; Ibata et al. 2001). Since these processes directly link morphology to galactic evolutionary histories, studying galaxy morphology becomes crucial for uncovering the physical mechanisms behind their formation and evolution.

Among various morphological features, structural asymmetries provide particularly valuable insights into the dynamical and evolutionary states of galaxies. Such asymmetries can arise from internal instabilities or external perturbations, revealing ongoing processes that shape disk evolution. A notable manifestation of these asymmetries is the presence of warped disks, which are characterized by systematic vertical displacements of the stellar and gaseous components from an ideal flat plane, typically with amplitudes of a few degrees. This

phenomenon has been observed in our Galaxy (e.g., Burke 1957; Jónsson & McMillan 2024; Kerr 1957; Djorgovski & Sosin 1989; Nurhidayat et al. 2020; Hunt & Vasiliev 2025) and in many galaxies in the local Universe (e.g., Reshetnikov 1995; Reshetnikov & Combes 1998a; García-Ruiz et al. 2002; Saroon & Subramanian 2022). Briggs (1990) provided a comprehensive summary and classification of the observed characteristics of galactic warps. Moreover, recent observations suggest that warp frequencies increase with redshift (Reshetnikov et al. 2025), implying an evolving nature of disk asymmetries over cosmic time.

These observational results highlight that warps are a common and long-lived feature in disk galaxies, yet the physical mechanisms responsible for their origin and longevity remain to be fully understood. Proposed explanations include internal bending instabilities (Sellwood 1996; Binney 1992), misaligned dark matter halos (Sparke & Casertano 1988; Debattista & Sellwood 1999; Han et al. 2023a,b), satellite interactions (Weinberg 1998; Laporte et al. 2018; Binney 2024), and ongoing cosmic gas accretion (Roškar et al. 2010; van de Voort et al. 2015). Several studies have also highlighted a possible link between environmental density and the presence of warps, with more strongly warped galaxies often found in denser regions (Reshetnikov & Combes 1998b).

The unclear origin of galactic warps is partly due to the small and non-uniform samples available, which limit reliable statistical analyses of their connection to galaxy structure and environment (e.g., García-Ruiz et al. 2002; Sánchez-Saavedra et al. 2003; Ann & Park 2006; Skryabina et al. 2024; Reshetnikov et al. 2025). To bridge this gap, we carry out a comprehensive analysis based on the DESI Legacy Imaging Surveys (DR8). The wide sky coverage, imaging depth, and relatively high resolution of the survey make it possible to identify a large number of warped galaxy candidates. Using a machine learning classifier applied to edge-on disk galaxies from the Galaxy Zoo DESI catalog, we identify 23,996 highly-confidence warped and 288,562 non-warped galaxies out of a total of 595,651 edge-on disk galaxies. We find statistical differences across several galaxy properties, including stellar mass, gas fraction, color, star formation rate, and disk morphology such as bulge prominence and disk size. These differences suggest that the presence of warps is linked to systematic variations in the structural and stellar characteristics of disk galaxies.

This paper is organized as follows. Section 2 introduces the dataset, explains how the sample was selected, and describes the training process of the machine learn-

ing model. In Section 3 we analyze the systematic differences in various properties between warped and non-warped edge-on-disk galaxies predicted by our classifier. Finally, in Section 4, we summarize our findings and discuss their implications for understanding the nature of galactic warps. We note that both the training and prediction processes are based solely on optical imaging, without incorporating morphological features of the gaseous disk.

## 2. METHODOLOGY

### 2.1. Surveys and Data

The Dark Energy Spectroscopic Instrument Legacy Imaging Surveys (DESI-LS) provide high-quality, wide-field optical imaging, enabling the detection of faint structural features such as spiral arms, bars, tidal debris, and disk warps. It is composed of three individual surveys: the Dark Energy Camera Legacy Survey (DECaLS), the Beijing-Arizona Sky Survey (BASS), and the Mayall z-band Legacy Survey (MzLS). BASS and MzLS (jointly referred as BASS/MzLS) together cover the Northern Galactic Cap (NGC) from Kitt Peak, USA; using the Bok 2.3-meter and Mayall 4-meter telescopes. DECaLS uses the 4-meter Blanco telescope at Cerro Tololo Inter-American Observatory equipped with the Dark Energy Camera (DECam; Flaugher et al. (2015)) to image the Southern Galactic Cap (SGC) and the  $\delta \leq 34^\circ$  region of the NGC. The combination of DECaLS and BASS/MzLS provides 14,000  $deg^2$  grz imaging data for DESI targeting. Notably, the Dark Energy Survey (DES) is conducted using the same instrument as DECaLS, so its imaging data are also included in the DESI Legacy Surveys Data Release 8 (DR8). Together, these four surveys, DECaLS, BASS, MzLS, and DES, provide a combined sky coverage of 19,437  $deg^2$ .

To ensure uniformity across the entire footprint, the imaging properties of these four surveys are similar by design, including depth and quality of the image across all components (Dey et al. 2019). The median coadded depths ( $5\sigma$  detection of a point source) reach approximately  $g = 24.2$ ,  $r = 23.8$ , and  $z = 23.3$  for BASS/MzLS, and  $g = 24.8$ ,  $r = 24.2$ , and  $z = 23.4$  for DECaLS. DES DR2 provides a median coadded catalog depth of  $g = 24.7$ ,  $r = 24.4$ , and  $z = 23.1$  for a  $1''.95$  diameter aperture in signal-to-noise ratio = 10.

The uniform, deep and wide imaging of these surveys enables large-scale morphology classification by training deep learning models on volunteer-labeled subsets and applying them to the remaining images. Walmley et al. (2021) presented the Galaxy Zoo DECaLS project, the first to produce a large-scale catalog of morphological measurements for all Galaxy Zoo questions

by training deep learning algorithms on citizen scientist classifications. They trained their model on DECaLS images using volunteer labels for various morphological features from the Galaxy Zoo website and then made the corresponding predictions. This catalog provided high-accuracy morphological classifications for over 314,000 galaxies from the DECaLS imaging surveys DR5 and within the SDSS DR8 footprint.

Building on the uniformly deep and consistent imaging dataset, [Walmsley et al. \(2023\)](#) extended the Galaxy Zoo morphological classification to the full DESI-LS footprint, expanding the sky coverage from about 5000 to over 19,000 deg<sup>2</sup>, covering nearly the entire extragalactic sky and enabling synergy with other major surveys such as ALFALFA and MaNGA. The released Galaxy Zoo DESI catalog includes fainter ( $r < 19.0$  vs.  $r < 17.77$ ), smaller, and higher-redshift (up to  $z \lesssim 0.4$  vs.  $z < 0.15$ ) galaxies compared to Galaxy Zoo DECaLS. Galaxies were selected with  $r < 19.0$  (to ensure sufficient resolution for visual morphology), surface brightness  $\mu > 18$  mag arcsec<sup>-2</sup>, and non-PSF profiles (based on the Tractor catalog), yielding an initial sample of 8,956,477 sources. After discarding images with more than 20% missing flux in any band, 8,689,370 galaxies remained as the final sample. For these galaxies, automated morphology predictions were released, providing the predicted fraction of volunteer responses for each Galaxy Zoo question, typically accurate to within 5–10% for each possible answer.

## 2.2. Sample Selection

Since our warp identification relies on optical imaging, we restrict our sample to edge-on galaxies, where the vertical displacement of the disk caused by warps is clearly observable. In less inclined galaxies, such distortions are largely hidden along the line of sight, making warp detection in optical images difficult. Following the recommended value in Table 2 of [Walmsley et al. \(2021\)](#), we selected sources from the Galaxy Zoo DESI catalog by applying a threshold of `edge-on_yes_fraction`  $\geq 0.8$ . Applying this selection criteria, we obtained a sample 595,651 of edge-on disk candidates. Then we downloaded cutout images of each source using the DESI-LS cutout service. Cutout images were obtained at a fixed pixel scale of 0.262 arcsec/pixel, with view sizes tailored to each galaxy’s angular size (see Appendix A). To maintain consistent coverage across the dataset, our view size selection ensures that most edge-on galaxies fill a similar proportion of the cutout. This helps preserve the outer disk regions, even in galaxies with large bulges and concentrated central light.

We also utilize several other morphological fractions predicted from Galaxy Zoo DESI classifications to characterize the structural and merger-related properties of galaxies. These include, for example, `merging_minor-disturbance_fraction`, `merging-none_fraction`, and bulge-size related fractions such as `bulge-size_small_fraction` and `bulge-size_moderate_fraction`. The definitions and physical meanings of all such parameters used in this work are summarized in Table 1.

## 2.3. Training Dataset Construction

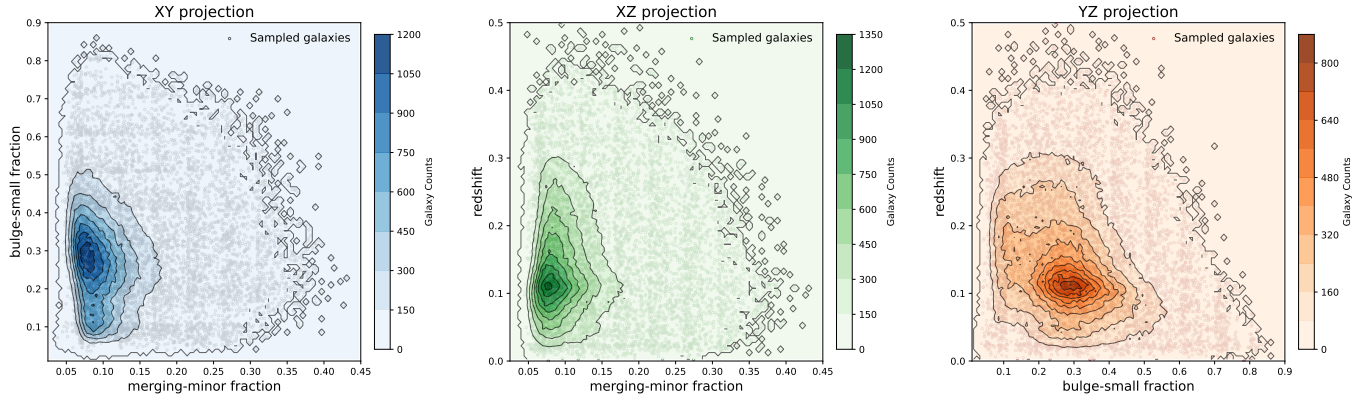
During the construction of the training and validation sets, one of the main challenges we encountered was the identification of a sufficient number of well-labeled warped galaxies, those exhibiting one-sided (U-shape) or two-sided (S-shape) warps, since such systems are relatively rare among edge-on galaxies when identified solely from optical-band images without accounting for gas-disk distributions. Moreover, warp features are also difficult to simulate or inject into real galaxy images without introducing unrealistic artifacts. For these reasons, we used visually identified real galaxies as positive warp examples to ensure morphological fidelity.

Initially, we suspected that the morphological signatures of disk warps might be partly interpreted by the Galaxy Zoo DESI model as minor disturbances or asymmetries. Therefore, we examined edge-on galaxies with relatively high `merging_minor-disturbance_fraction` values to search for potential warped systems that could have been classified as such by the machine predictions. We indeed found that warp-like features often exist among these galaxies, highlighting the potential of identifying a large number of warped systems in the optical bands. However, to ensure that the final training set was unbiased and representative of the full diversity of galaxy properties, we adopted a three-dimensional binned sampling strategy (see Figure 1). Specifically, we binned all edge-on galaxies in the parameter space of `merging_minor-disturbance_fraction`, `bulge-size_small_fraction`, and redshift, and then randomly selected 20 galaxies from each bin for labeling, or included all galaxies in bins containing fewer than 20 objects. This approach ensured that rare types of galaxies were adequately represented and prevented sampling bias toward more numerous systems. Labeling was performed by a single annotator, with ambiguous cases excluded, and clear criteria and high-resolution images were used to maintain consistency.

Finally, our labeled set consists of 2225 positive samples (S-shaped and U-shaped warped galaxies) and 3580 negative samples (non-warped edge-on galaxies). We

**Table 1.** Predicted morphological parameters based on Galaxy Zoo DESI classifications. All fractions are in the range  $[0, 1]$ .

Parameter	Physical Meaning
<code>edge-on_yes_fraction</code>	Predicted fraction (0–1) of votes classifying the galaxy as edge-on.
<code>merging_minor-disturbance_fraction</code>	Predicted fraction (0–1) of votes indicating minor disturbances, likely due to a minor merger.
<code>merging-none_fraction</code>	Predicted fraction (0–1) of votes indicating no signs of merging or disturbance.
<code>bulge-size_small_fraction</code>	Predicted fraction (0–1) of votes classifying the galaxy’s bulge as small relative to total stellar mass or light.
<code>bulge-size_moderate_fraction</code>	Predicted fraction (0–1) of votes classifying the galaxy’s bulge as moderate in size.

**Figure 1.** Three two-dimensional projections of edge-on galaxies in the parameter space of `merging_minor-disturbance_fraction`, `bulge-size_small_fraction`, and redshift. Contours indicate the distribution of all edge-on galaxies in each projected plane, and scatter points show the subset selected for labeling using our 3D binned sampling strategy, with up to 20 galaxies randomly drawn per bin. This approach ensures that rare types of galaxies are represented, improving the completeness and diversity of the training set.

randomly split the data into 80%, 10%, and 10% for training, validation, and testing, respectively. Figure 2 illustrates a representative subset of the galaxies used for training the warp classification model, with non-warped examples shown in the top panel and warped examples in the bottom panel.

#### 2.4. Data Preprocessing and Model Training

We adopt the EfficientNet-B3 architecture (Tan & Le 2019) as the backbone of our classification model. EfficientNet employs a compound scaling method that uniformly adjusts network depth, width, and input resolution, achieving high accuracy with relatively low computational cost. The B3 variant provides an optimal balance between model capacity and efficiency, with approximately 12 million parameters and an input resolution of  $300 \times 300$  pixels. We initialize the network with ImageNet-pretrained weights, enabling effective transfer learning by leveraging features learned from a large and diverse dataset. This allows the model to capture both low-level textures, such as local brightness gradients and subtle edge distortions, and higher-level structural features, including the global shape and orientation of galaxy disks.

To increase diversity and reduce overfitting, we applied a series of data augmentation techniques to the galaxy images. The images were resized to  $300 \times 300$  pixels and randomly flipped horizontally. We also applied random rotations up to  $45^\circ$ , and color jittering with moderate adjustments in brightness, contrast saturation, and hue. Finally, the images were converted to tensors and normalized with a mean of 0.05 and a standard deviation of 0.1. The model training was optimized using Optuna (Akiba et al. 2019), which searched for the best hyperparameters within a predefined range to maximize performance. The search space included learning rate, dropout, class weight, and batch-size. We also experimented with a gradual unfreezing strategy—training only the classification head first and progressively unfreezing deeper layers—but found that it had little effect on the model performance. For the final model training, we used a batch size of 32 and trained for 100 epochs. Class weights were set to  $[1.0, 1.0]$ , and a dropout rate of 0.297 was applied to prevent overfitting. The model was optimized using the AdamW optimizer with a learning rate of  $1.7 \times 10^{-4}$  and a weight decay of  $1.0 \times 10^{-2}$ .

We saved models from all epochs and selected the one with best performance on the test set as the final model.

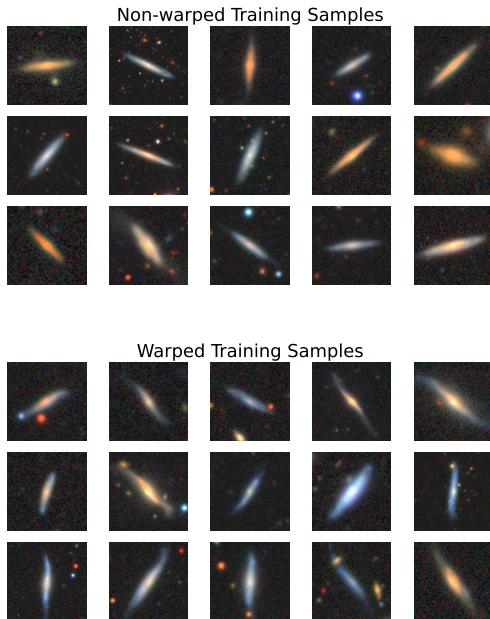


**Figure 2.** The figure shows example galaxy images used for training. The top panel shows non-warped galaxies, and the bottom panel shows warped galaxies.

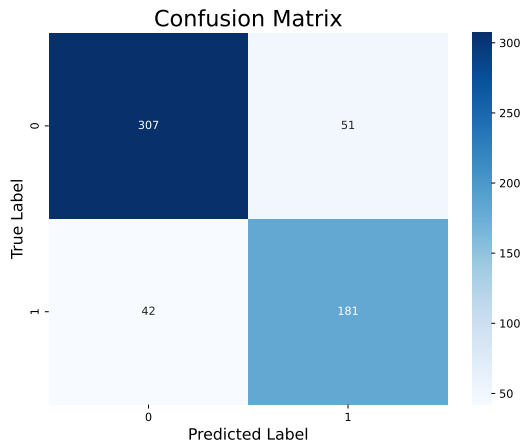


**Figure 3.** Confusion matrix of the best-performing model among all saved epochs.

The corresponding confusion matrix for the best model is shown in Figure 3, illustrating how predictions are distributed across the two classes.

The evaluation metrics used in Table 2 are defined as follows. We denote one class as the positive class ( $P$ ) and the other as the negative class ( $N$ ). In our study,

Class	Precision	Recall	F1-score	Support
0	0.88	0.86	0.87	358
1	0.78	0.81	0.80	223
Accuracy	0.84			
Macro Avg	0.83	0.83	0.83	581
Weighted Avg	0.84	0.84	0.84	581

**Table 2.** Precision, recall, F1-score, and support for each class on the test set. This corresponds to the best-performing model among all saved epochs.

the positive class corresponds to warped galaxies. We define:

- $TP$ : number of positive samples correctly predicted as positive.
- $FP$ : number of negative samples incorrectly predicted as positive.
- $FN$ : number of positive samples incorrectly predicted as negative.
- $TN$ : number of negative samples correctly predicted as negative.

Based on these, the metrics for the positive class are

$$\begin{aligned} \text{Precision}_P &= \frac{TP}{TP + FP}, \\ \text{Recall}_P &= \frac{TP}{TP + FN}, \\ \text{F1-score}_P &= \frac{2 \text{Precision}_P \text{Recall}_P}{\text{Precision}_P + \text{Recall}_P}, \\ \text{Support}_P &= TP + FN. \end{aligned}$$

Similarly, the metrics for the negative class can be computed by swapping  $P$  and  $N$ .

The overall accuracy is

$$\text{Accuracy} = \frac{TP + TN}{TP + TN + FP + FN}.$$

The macro-averaged and weighted-averaged metrics across the two classes are

$$\begin{aligned} \text{Macro Avg} &= \frac{\text{metric}_P + \text{metric}_N}{2}, \\ \text{Weighted Avg} &= \frac{\text{Support}_P \cdot \text{metric}_P + \text{Support}_N \cdot \text{metric}_N}{\text{Support}_P + \text{Support}_N}, \end{aligned}$$

where  $\text{metric}_P$  and  $\text{metric}_N$  can be Precision, Recall, or F1-score.

The model achieves an overall accuracy of 84% on the test set (Table 2). For class 0, the precision, recall, and F1-score are 0.88, 0.86, and 0.87, respectively, indicating

a strong performance in identifying this class. For class 1, the precision recall and F1-score is 0.78, 0.81, and 0.80, showing slightly lower performance but still acceptable. The macro-averaged metrics are all 0.83, indicating balanced performance across classes. The weighted averages are similar to the overall accuracy.

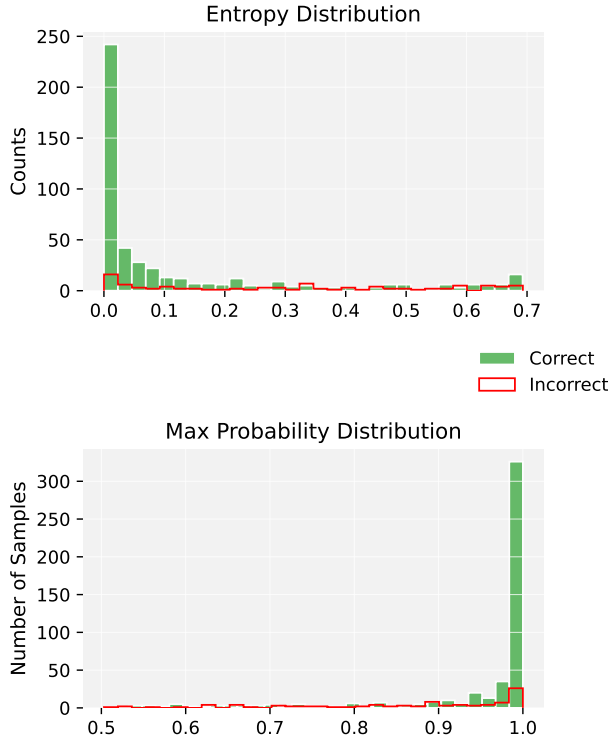


**Figure 4.** Correct predictions (green) tend to have high confidence and low uncertainty, while incorrect predictions (red) show the opposite pattern. This validates the use of these metrics for high-confidence selection.

To ensure a reliable final sample, we selected galaxies with a maximum predicted class probability  $p \geq 0.99$  and entropy  $H \leq 0.1$ . We chose these thresholds because correctly classified galaxies in the test set usually met these conditions (see Figure 4). This helps keep only those galaxies the model is confident about, removing uncertain cases. After applying this selection, the precision of class 0 and class 1 in the test dataset increased to 0.95 and 0.89, respectively.

Using this best-performing model, we applied predictions to 595,651 galaxies that have `edge-on_yes_fraction` greater than or equal to 0.8 from the Galaxy Zoo DESI catalog. Among them, galaxies satisfying the criteria of maximum predicted probability  $p \geq 0.99$  and entropy  $H \leq 0.1$  were selected as high-confidence warped and non-warped galaxies. This selection resulted in a final set of 23996 warped

and 288562 non-warped edge-on galaxies. A random subset of these high-confidence predictions is shown in Figure 5.

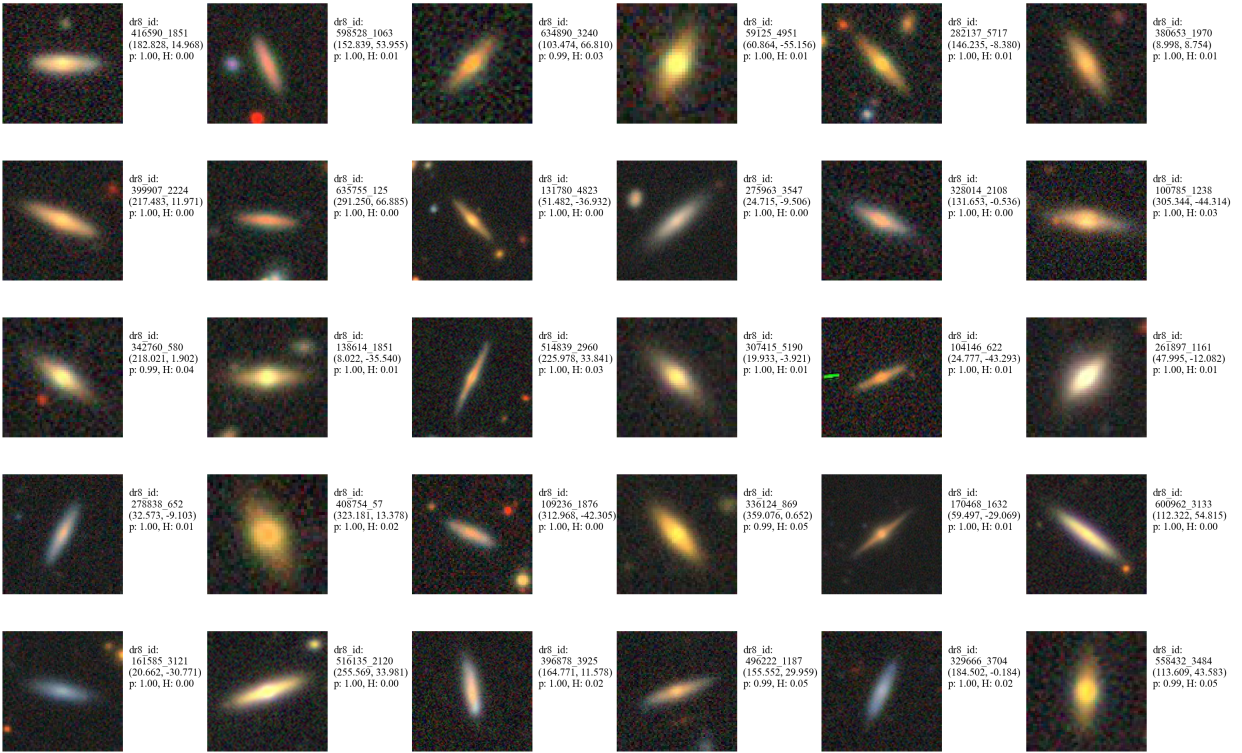
**Table 3.** Number of galaxies with valid measurements for morphological and physical properties.

Morphological Properties		
Property	Warped Galaxies	Non-warped Galaxies
Sérsic axis ratio	3372	29258
Physical size	3366	29228
Sérsic index	3372	29258
c	3372	29257
Bulge and merging relevant fractions	23996	288562
Physical Properties		
Property	Warped Galaxies	Non-warped Galaxies
$u - g$	3372	29254
$g - r$	3372	29256
$r - i$	3372	29255
$i - z$	3371	29252
HI mass	579	727
Stellar Mass	3372	29258
Gas Fraction	458	595
Rotation Speed	457	595
SFR median, SFR entropy, sSFR median, sSFR entropy	3111	28143

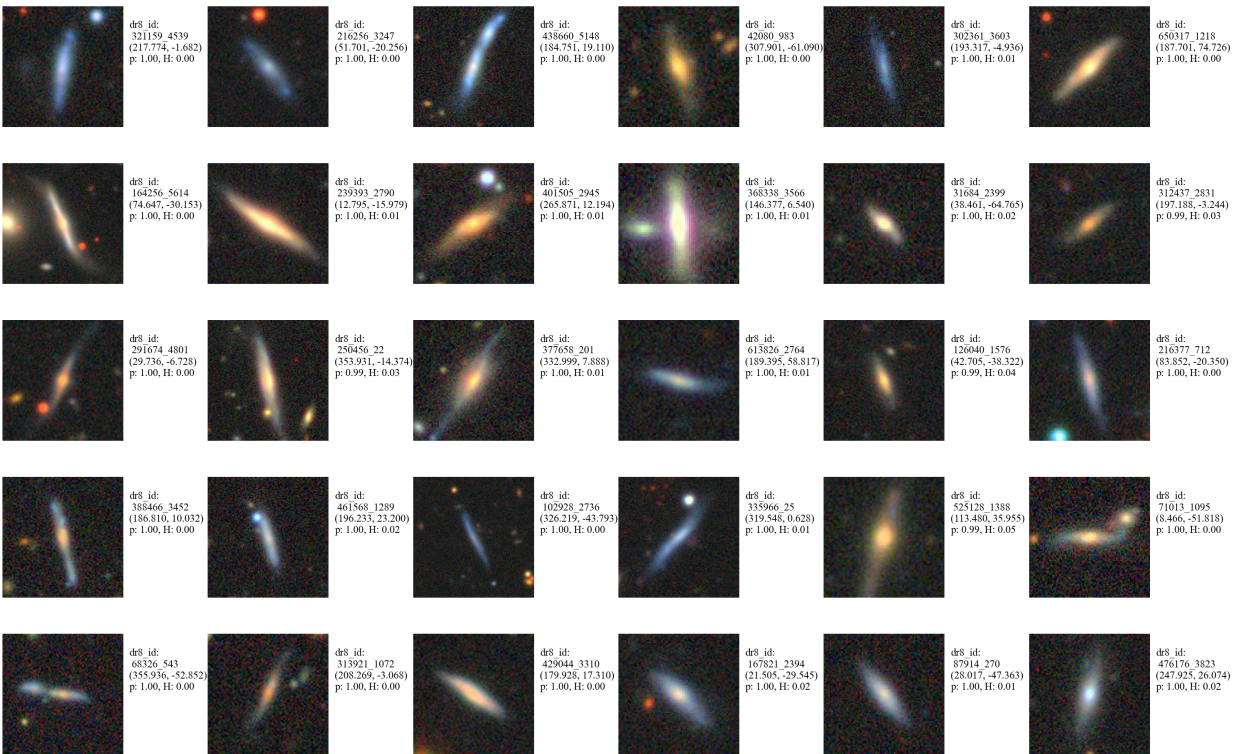
In addition to the main morphology catalog, [Walmsley et al. \(2023\)](#) also released an external catalog, which includes cross-matched properties from other surveys (e.g., [Aguado et al. 2019](#); [Haynes et al. 2018](#); [Abazajian et al. 2009](#); [Zhou et al. 2021](#)). Using the `dr8_id`, we matched our classified galaxies to this external catalog and obtained a variety of galaxy properties, including photometry in the  $g$ ,  $r$ , and  $z$  bands, stellar mass, size, axial ratio, Sérsic index, HI mass, star formation rate and other relevant properties. To investigate the environmental context of our galaxies, we performed a cross-match with the SDSS DR7 group catalog ([Yang et al. 2007](#)) using a 2 arcsecond radius. All galaxies were uniquely matched to a single group, providing a clean sample for subsequent analysis of both intrinsic and group-related properties; approximately 79% of the galaxies are central members.

Table 3 summarizes the number of galaxies with valid measurements for each morphological, physical, and star formation property. Based on these measurements, we

## Non-warped Predictions



## Warped Predictions



**Figure 5.** Images of randomly selected galaxies with high-confidence model predictions: the top panel shows non-warped galaxies, and the bottom panel shows warped galaxies.

can now compare the structural properties of warped and non-warped galaxies.

### 3. RESULTS

#### 3.1. *Morphological properties*

We find that the axis ratios (b/a) of warped edge-on disk galaxies are largely comparable to those of non-warped ones (Figure 6, top panel), suggesting that the occurrence of warps is not strongly related to the axis ratio itself. In contrast, warped galaxies exhibit significantly larger effective radii (Figure 6, top panel), which indicates that galaxy size might play a significant role in the occurrence of warps. One possible explanation is that larger galaxies are either intrinsically more susceptible to warp formation due to weaker self-gravity at their outskirts, or that warps in larger systems are easier to detect observationally. Further investigation considering stellar mass, environment, and disk structure is required to disentangle intrinsic physical factors from observational biases. No significant difference between warped and non-warped galaxies is seen in the concentration parameter calculated as `petro_th90/petro_th50` (Figure 6, top panel). This lack of contrast is likely because the warped regions are located in the faint outer parts of the disk, to which `petro_th90` is relatively insensitive.

We also find that warped disk galaxies exhibit systematically lower Sérsic indices compared to non-warped ones (Figure 6, top panel). Although some warped galaxies also show prominent bulges, the overall trend indicates that warps are more common in systems with lower Sérsic indices. The Sérsic index, a measure of the concentration of a galaxy’s light profile, is relatively unaffected by viewing angle in large samples, and therefore serves as a robust proxy for intrinsic morphology. Lower Sérsic indices are generally associated with disk-dominated galaxies, which are more responsive to gravitational perturbations and thus more likely to exhibit warps.

Consistent with this view, we examined several morphological predictions from the Galaxy Zoo DESI project, focusing on bulge and merger-related fractions. We find that warped edge-on disk galaxies generally exhibit smaller bulges than their non-warped counterparts, as indicated by systematically higher values in the predicted `bulge-size_small_fraction` and lower values in `bulge-size_moderate_fraction`. These trends suggest that warps predominantly occur in disk-dominated galaxies with relatively small. Warped galaxies also showing lower `merging_none_fraction` and higher `merging_minor-disturbance_fraction` (Figure 6, bottom panel). However, caution is required when

interpreting the link between warps and minor mergers, since the `merging_minor-disturbance_fraction` is based on visual features. The elevated `merging_minor-disturbance_fraction` among warped galaxies may primarily reflect their morphological irregularities rather than direct evidence of ongoing mergers.

#### 3.2. *physical properties*

Our result reveals clear physical differences between warped and unwarped galaxies. Overall, warped edge-on disk galaxies tend to be bluer in color, less massive, and more gas-rich (see Figure 7). These characteristics are typically associated with younger, star-forming systems. In contrast, edge-on disk galaxies without warps are generally redder, more massive, and gas-poorer, indicative of more evolved systems with lower star formation activity.

On average, non-warped galaxies are redder than warped galaxies, with higher  $u - g$  and  $g - r$  values. The differences in  $r - i$  and in  $i - z$  are almost negligible (Figure 7, top panel). In general, the color contrast is more pronounced at shorter wavelengths, as seen in the larger difference in  $u - g$  and  $g - r$  compared to  $r - i$  and  $i - z$ . This indicates that the observed differences primarily reflect variations in the light from relatively younger stellar populations, while the contributions from older stars traced by longer-wavelength colors are similar. While these color differences alone cannot unambiguously indicate the current star formation activity, warped galaxies do exhibit higher star formation rates, as illustrated in the last panel of Figure 7.

Among disk galaxies successfully cross-matched with ALFALFA observations, we compared the HI gas content of warped and non-warped systems. We find that warped galaxies exhibit slightly higher HI masses compared to their non-warped counterparts, while their stellar masses are significantly lower. As a result, warped galaxies have systematically higher gas fractions. This trend suggests that warped galaxies are generally more gas-rich and less evolved on average in terms of stellar mass assembly (Figure 7, middle panel). It is worth noting, however, that the ALFALFA survey is subject to strong selection effects: only galaxies with sufficiently high HI content can be detected. Therefore, the non-warped galaxies included in this comparison represent the gas-rich, star-forming population, rather than the entire non-warped sample. Consequently, the difference in gas fraction between warped and non-warped galaxies may be even more pronounced when considering the full galaxy population. We also compared the overall probability distribution functions of rotational velocities for warped and non-warped galaxies, and found the distri-

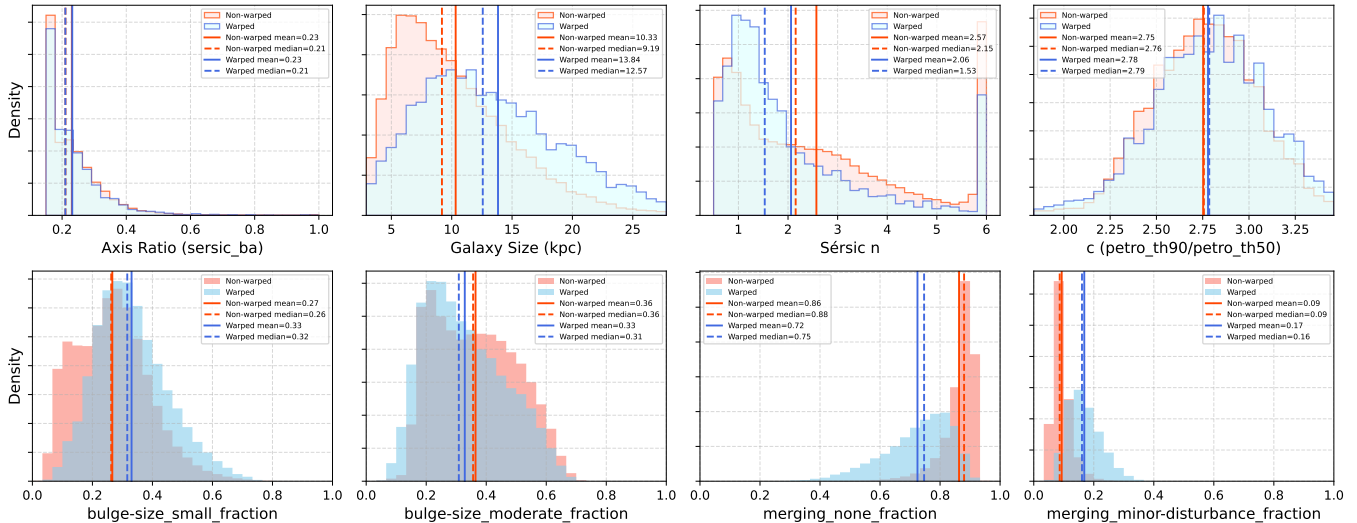


**Figure 6.** Comparison of morphological properties between warped and non-warped edge-on galaxies. **Top row:** distributions of Sérsic axis ratio ( $b/a$ ), galaxy size (computed from `elpetro.theta_r`) in physical units (kpc), Sérsic index ( $n$ ), and concentration ( $c$ , `petro.th90/petro.th50`). Redshifts used for physical size calculation include both spectroscopic and photometric measurements. **Bottom row:** distributions of bulge size fractions (small and moderate) and merging fractions (none and minor-disturbance). Warped galaxies are shown in blue, non-warped galaxies in red. Vertical solid and dashed lines indicate the mean and median of each sample, respectively. All histograms are normalized to show probability density.

butions to be comparable. The rotational velocities were estimated from HI line widths corrected for inclination using Sérsic axis ratios, so the accuracy for individual galaxies is limited.

We further investigated the star formation properties of warped versus non-warped galaxies and found that warped galaxies exhibit systematically higher star formation rates (SFR), specific star formation rates (sSFR), and higher SFR entropy. The PDF of  $\log(\text{sSFR})$  for edge-on galaxies in the non-warped sample exhibits a clear bimodal distribution, with one peak around typical star-forming values and another significant peak at  $\log(\text{sSFR}) < -11$  (Figure 7, bottom panel). This low-sSFR peak indicates that a fraction of these galaxies have already quenched, likely transitioning into a quiescent or passive state, whereas the majority of warped edge-on galaxies remain actively star-forming. Also, the SFR/sSFR entropy values of warped galaxies are generally higher, indicating a broader distribution of star formation activity, whereas non-warped galaxies show a pronounced peak at relatively low entropy values.

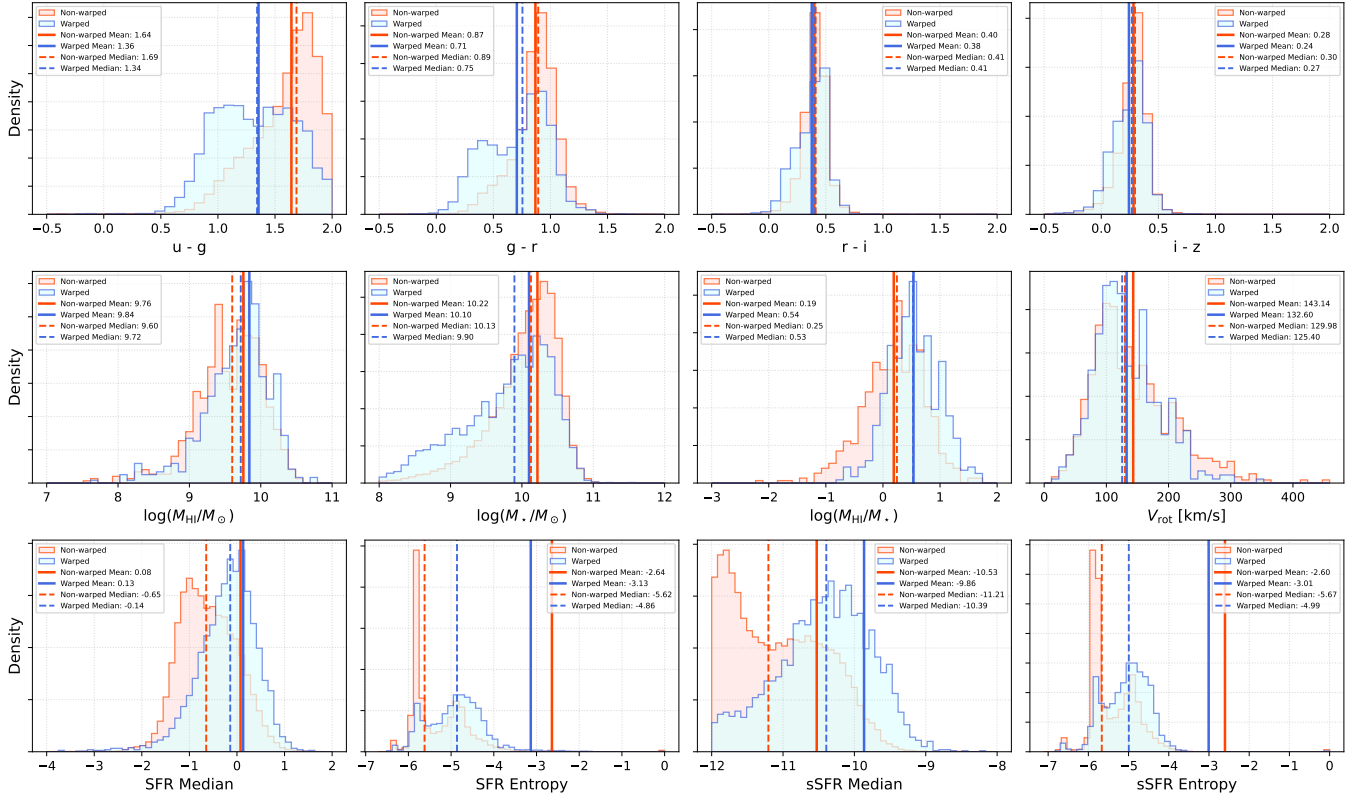
### 3.3. Dependence on Galaxy Masses

Many galaxy properties are strongly correlated with stellar mass. To ensure that the differences we observe between warped and non-warped galaxies reflect the impact of warps rather than underlying mass trends, we control for stellar mass in our analysis, by comparing galaxies within similar stellar mass bins.

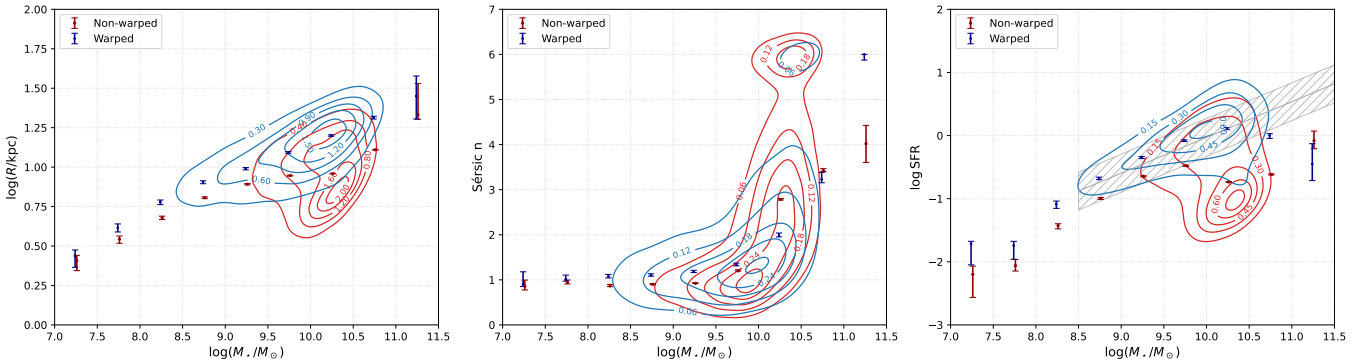
As have been shown earlier, warped galaxies have, on average, larger physical sizes (Figure 6). However, their stellar masses are generally lower (Figure 7). The 2D mass–size distribution reveals that warped galaxies are more widely dispersed across the plane than non-warped ones; within the same mass range, they tend to have larger sizes (Figure 8). Dividing the sample into stellar mass bins, we further found that warped galaxies exhibit larger median sizes than non-warped galaxies across all mass bins, and the size difference between warped and non-warped galaxies becomes more pronounced at higher stellar masses. This trend supports that the occurrence of warps is likely related to the structure of the outer stellar disk, where more extended or less tightly bound outer regions could be more susceptible to warping. In contrast, many high-mass non-warped galaxies may be bulge-dominated, which contributes to the observed size difference.

Figure 8 shows that warped galaxies tend to exhibit lower Sérsic indices at fixed stellar mass compared to non-warped counterparts at intermediate masses ( $\log(M_*/M_\odot) \sim 10.0 - 11.0$ ), suggesting that warped systems are generally more disk-dominated. At the low- and high-mass ends, the differences between the two populations are less pronounced, and in some cases the trend even appears to reverse. Overall, this trend is consistent with warped galaxies preferentially residing in late-type, disk-dominated systems.

The 2D distribution on the stellar mass–SFR plane (Figure 8) shows that at all stellar mass ranges, the



**Figure 7.** This figure illustrates the differences in physical properties between galaxies. The first row shows the color indices ( $u - g$ ,  $g - r$ ,  $r - i$ , and  $i - z$ ). The second row presents gas mass, stellar mass, gas fraction, and rotational velocity. The third row displays the median and entropy of star formation rate (SFR) and specific star formation rate (sSFR). Vertical solid and dashed lines indicate the mean and median of each sample, respectively. All histograms are normalized to show probability density.



**Figure 8.** Density distributions of key physical and structural properties as a function of stellar mass for warped (blue) and non-warped (red) disk galaxies. Each panel shows kernel density contours of the two populations, with binned medians and corresponding  $1\sigma$  uncertainties overplotted as symbols. From left to right and top to bottom, the panels show: (a) Disk Size  $R$  (kpc), (b) Sérsic index  $n$ , (c) star-formation rate (SFR). The gray line in panel (c) denotes the star-forming main sequence from Speagle et al. (2014), with the shaded region indicating its  $\pm 0.3$  dex intrinsic scatter.

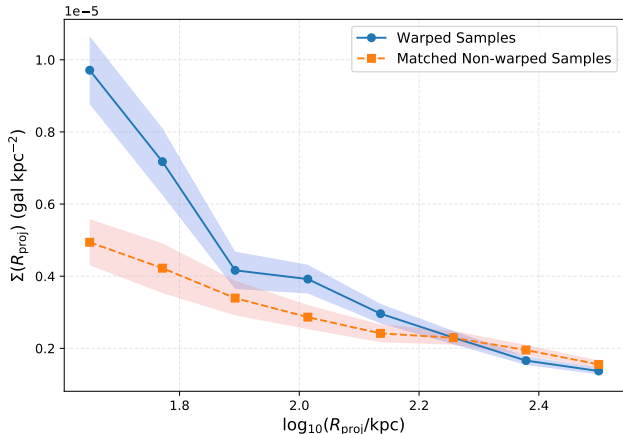


**Figure 9.** Projected neighbor surface density profiles,  $\Sigma(R_{\text{proj}})$ , for warped (blue) and matched non-warped (red) galaxies as a function of projected separation  $R_{\text{proj}}$  (in kpc). Solid circles and blue shading denote the mean and standard error of the mean (SEM) for warped galaxies, while dashed squares and red shading show the corresponding values for matched non-warped control samples. Warped galaxies exhibit systematically higher local projected densities at small separations.

median SFR of warped galaxies remains higher than that of non-warped galaxies. The result further supports the trend in sSFR distribution (Figure 7): warped edge-on galaxies rarely appear in the quenched region and are predominantly located along, or slightly above, the star-forming main sequence, exhibiting systematically higher SFRs than both the main sequence average and their non-warped counterparts. Notably, quenched galaxies are almost entirely absent from the warped population. In contrast, non-warped galaxies show a broader spread, with a significant fraction lying below the main sequence—indicative of quenching activity.

### 3.4. Environmental Difference

To minimize the influence of other confounding factors, we applied a matched-control strategy to the warped galaxies by searching for their nearest non-warped counterparts in the parameter space of stellar mass, color, and redshift. Given that the ratio between high-confidence warped and non-warped galaxies is approximately 1:10, we selected seven non-warped counterparts for each warped galaxy that closely match in stellar mass, color, and redshift. Since only galaxies within the SDSS survey volume have reliable stellar mass measurements, we further cross-matched our sample with the SDSS DR7 group catalog from Yang et al. (2007) to investigate their environmental properties. For each galaxy, a counterpart was identified within a two arcsecond matching radius.

We quantify the local environmental densities around warped galaxies and their non-warped matched counterparts by computing the *projected surface number density* of neighboring galaxies within concentric annuli, defined as

$$\Sigma(R_{\text{proj}}) = \frac{N(R_i < R_{\text{proj}} < R_{i+1})}{\pi (R_{i+1}^2 - R_i^2)},$$

where  $R_{\text{proj}}$  denotes the projected separation from the target galaxy on the sky. This annular measurement traces the spatial distribution of neighboring galaxies as a function of scale. To select neighboring galaxies within each annulus, we apply a line-of-sight constraint based on redshift. The maximum allowed redshift difference is

$$\Delta z_{\text{max}} = \frac{\Delta v_{\text{max}}}{c} (1 + z_{\text{target}}),$$

where  $\Delta v_{\text{max}} = 500 \text{ km s}^{-1}$  and  $c$  is the speed of light. Only galaxies with  $|z_{\text{neighbor}} - z_{\text{target}}| \leq \Delta z_{\text{max}}$  are counted as neighbors, minimizing contamination from foreground or background objects along the line of sight.

As shown in Figure 9, warped galaxies (blue) tend to have higher annular surface densities than their matched non-warped counterparts (red) at small to intermediate projected radii. The difference is especially pronounced within  $\log_{10}(R_{\text{proj}}/\text{kpc}) \lesssim 1.7$  ( $R_{\text{proj}} \lesssim 50 \text{ kpc}$ ), where the local number density around warped galaxies is roughly twice as high as that around non-warped galaxies. This trend indicates an association between disk warping and denser immediate environments, although it is unclear whether the environment directly induces warps or merely traces other galaxy properties linked to warping. At larger projected separations ( $R_{\text{proj}} \gtrsim 200 \text{ kpc}$ ), the two profiles converge, implying that any connection between disk warping and environment is more likely limited to the local, small-scale surroundings. We note, however, that these measurements only consider the projected surface density of neighboring galaxies; more detailed studies, including kinematic information and three-dimensional environmental reconstruction, will be required to establish whether local interactions play a causal role in inducing disk warps.

## 4. SUMMARY

By applying a convolutional neural network classifier to edge-on disk galaxy images from the DESI DR8 Legacy Imaging Surveys, we constructed the largest catalog of warped galaxies to date, enabling statistical comparisons between warped and non-warped systems for the first time. This work is based solely on optical imaging data, with the sample restricted to edge-on disk galaxies to ensure reliable identification of warps. The result reveals that these warped edge-on galaxies exhibit

notable morphological, physical, and environmental differences compared to their non-warped counterparts.

Morphologically, warped galaxies tend to have larger disks, lower bulge-relevant fractions, and higher merging-relevant fractions, consistent with late-type, disk-dominated structures that may be more susceptible to warping. Their axis ratios are comparable to those of non-warped galaxies, indicating similar overall flattening. When dividing galaxies into stellar mass bins, warped galaxies exhibit larger median sizes than non-warped galaxies across all bins, with the difference becoming more pronounced at higher stellar masses. The trend indicates that warps may be associated with the structure of the outer stellar disk, where extended or loosely bound outer regions could be more prone to warping, whereas high-mass non-warped galaxies tend to be bulge-dominated, contributing to the size disparity. Overall, non-warped galaxies exhibit higher Sérsic indices than warped ones; this trend is primarily driven by the intermediate-mass range, where a pronounced peak around  $n \sim 6$  reflects a population of bulge-dominated systems. At lower and higher masses, by contrast, warped galaxies tend to show comparable or even slightly higher Sérsic indices.

Physically, warped galaxies tend to be less massive, bluer, and more gas-rich than their non-warped counterparts. The color difference between warped and non-warped galaxies is particularly pronounced at shorter wavelengths, consistent with their higher SFRs, reflecting more active star formation in warped galaxies, while at the longest wavelengths the two populations show little color distinction. On the stellar mass–SFR plane, warped galaxies largely follow the star-forming main sequence, often lying slightly above it, indicative of active star formation and mildly elevated SFRs compared to the average star-forming population. In contrast, many non-warped galaxies fall below this sequence, suggesting they are quenched or transitioning into quiescence, a distinction reinforced by the sSFR distribution, where non-warped galaxies exhibit a bimodal pattern with a prominent low-sSFR peak below  $\log(\text{sSFR}) \approx -11$ , characteristic of quenched systems. It should be noted that our sample selection is based solely on the edge-on criterion `edge-on_yes_fraction`, and due to projection effects it is difficult to identify the presence of spiral arms in these systems; thus, the potential contribution of S0 galaxies with lower star formation cannot be fully excluded. Overall, warped galaxies generally appear to represent an earlier evolutionary stage compared to non-warped galaxies.

In terms of environmental properties, we find that warped galaxies tend to have a higher number of nearby companions than their non-warped counterparts, particularly within  $R_{\text{proj}} \lesssim 50$  kpc, where the local projected number density is roughly twice as high. At larger separations, the environmental difference disappears, indicating that warps preferentially reside in locally denser regions, although it remains unclear whether this reflects a causal effect or merely traces other environmental properties.

Together, these results suggest that disk warping is closely linked to the structural properties, star formation activity, and small-scale environments of galaxies, highlighting the interplay between internal dynamics and local interactions. Warps preferentially occur in late-type disk galaxies with larger galaxy sizes and less massive bulges, which are also more gas-rich and actively star-forming, and may be more susceptible to external torques or internal dynamical instabilities. They are more often found in denser local environments at small separations, suggesting a possible link between warps and interactions. However, establishing a direct causal connection requires more detailed observations, including stellar and gas kinematics, three-dimensional reconstructions of local environments, and deep imaging of faint outer disks. High-resolution simulations of galaxy interactions and gas accretion will also be essential to understand the physical mechanisms driving warp formation and their evolution over cosmic time.

1 This work made use of the publicly available data from  
 2 the Galaxy Zoo DESI project, the DESI Legacy Imag-  
 3 ing Surveys DR8, and the SDSS DR7 group catalog con-  
 4 structed and released by Xiaohu Yang and collaborators.  
 5 We would like to thank the Galaxy Zoo DESI team, the  
 6 DESI Legacy Imaging Surveys team, and the Shang-  
 7 hai Jiao Tong University group catalog team for making  
 8 their data products publicly available.

9 YHW thanks Houzun Chen and Ziyong Wu for helpful  
 10 discussions and suggestions.

11 This work is supported by the National Key Research  
 12 and Development Program (No. 2022YFA1602903, No.  
 13 2023YFB3002502), NSFC(No.12533007), the science re-  
 14 search grants from the China Manned Space project  
 15 with NO.CMS-CSST-2025-A10. JFL thanks research  
 16 grants from the National Natural Science Foundation  
 17 of China (No. 12403016) and the Postdoctoral Fellow-  
 18 ship Program of CPSF (No. GZC20241514). HYW is  
 19 supported by the National Natural Science Foundation  
 20 of China (NSFC, Nos. 12192224). EW thanks sup-  
 21 port of the National Science Foundation of China (Nos.  
 22 12473008).

## APPENDIX

## A. VIEW SELECTION CRITERIA

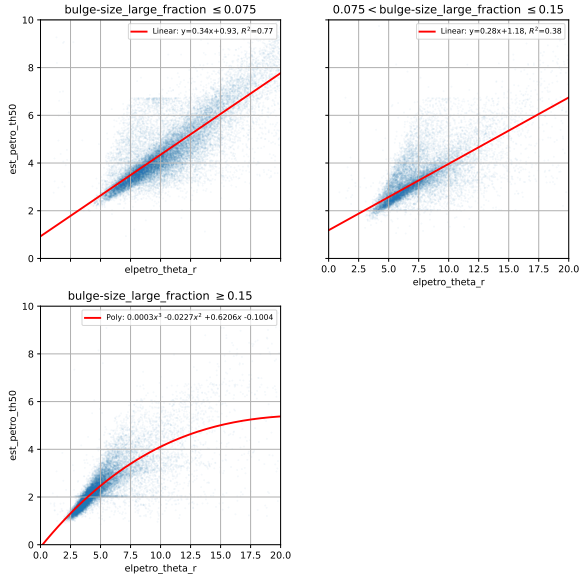


**Figure 10.** Correlation between estimated Petrosian half-light radius (`est_petro_th50`) and Petrosian angular size (`elpetro_theta_r`) for galaxies in different bulge-dominated regimes. The sample is divided into three bins of `bulge-size_large_fraction`:  $\leq 0.075$  (top left),  $0.075 < \text{fraction} \leq 0.15$  (top right), and  $\geq 0.15$  (bottom). Scatter points represent individual galaxies, while red curves show the best-fit relations. The correlation is tightest for the lowest bulge fractions, weakens for intermediate fractions, and becomes nonlinear for the most bulge-dominated systems.

To ensure that each cutout image captures the full structure of a galaxy while remaining focused on its morphology, an appropriate cutout size must be selected for each galaxy. We found that relying solely on the estimated Petrosian half-light radius (`est_petro_th50`) does not provide suitable sizes for all galaxies, particularly for edge-on systems with prominent bulges, where the galaxies’ angular sizes tend to be underestimated. While `elpetro_theta_r` offers a more reliable measure for setting the image scale, some galaxies in the Galaxy Zoo DESI catalog lack valid `elpetro_theta_r` values. For these cases, we estimate `elpetro_theta_r` from their available `est_petro_th50` values, using an empirical re-

lation derived from galaxies with both parameters measured.

We first investigated the relationship between the estimated Petrosian half-light radius (`est_petro_th50`) and the elliptical Petrosian radius (`elpetro_theta_r`). Galaxies were initially divided into three morphological subgroups according to their `bulge-size_large_fraction`, corresponding to disk-dominated, intermediate, and bulge-dominated systems. As illustrated in Fig. 10, the correlations between `est_petro_th50` and `elpetro_theta_r` differ across these subgroups: a robust linear relation is found for disk-dominated galaxies, a weaker and more scattered relation for intermediate systems, and a nonlinear trend better captured by a third-order polynomial for bulge-dominated galaxies. These empirical fits provide a basis for estimating `elpetro_theta_r` in cases where it is missing in the catalog.

For galaxies with `bulge-size_large_fraction`  $\leq 0.15$ , we set

$$\theta_r = 2 \times \text{est\_petro\_th50}$$

while for galaxies with larger bulges (`bulge-size_large_fraction`  $> 0.15$ ), we estimate  $\theta_r$  by inverting the polynomial relation calibrated in Fig. 10 when `est_petro_th50`  $\lesssim 5.6$ , and apply fixed upper bounds of  $\theta_r = 25$  or  $\theta_r = 30$  for more extended cases. The final cutout size is then defined as

$$\text{cutout\_size} = \text{round} \left( \frac{4 \times \theta_r}{\text{PIX\_SCALE}} \right)$$

Nevertheless, we found that in the intermediate bulge regime, a subset of galaxies exhibits significantly over-estimated values of `elpetro_theta_r`, which would result in excessively large image cutouts and hinder the subsequent machine-learning classification. To mitigate this, we adopted an alternative parameterization based on `bulge-size_small_fraction`, which provides a more practical morphological separation for our purpose.

## B. TRAINING VS. PREDICTED SAMPLE PROPERTIES

To verify the representativeness and reliability of our trained classifier, we compare the distributions of various physical properties between the original training samples and the predicted samples for both warped and non-warped galaxies (See in Figure 11). This comparison allows us to check whether the predicted samples

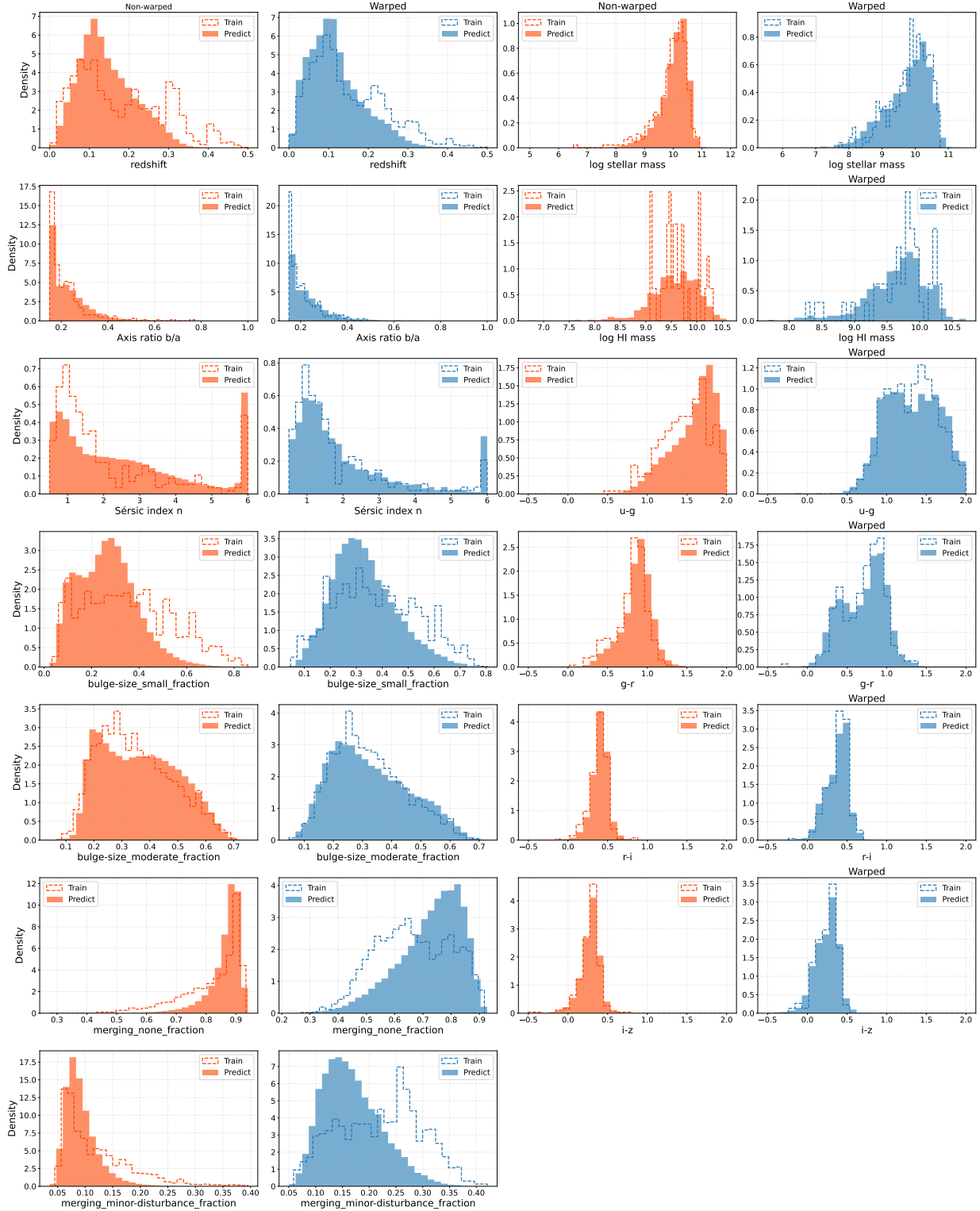


**Figure 11.** Comparison of distributions for various physical properties between the training and predicted samples of warped and non-warped galaxies. The left half (first two columns) shows seven physical quantities: redshift, axis ratio  $b/a$ , Sérsic index  $n$ , bulge fraction, bulge moderate fraction, merging none fraction, and merging minor disturbance fraction. The right half (last two columns) shows the remaining six quantities: log stellar mass, log HI mass, and four colors ( $u - g$ ,  $g - r$ ,  $r - i$ ,  $i - z$ ). Each row corresponds to a specific quantity, with the first column for non-warped galaxies and the second column for warped galaxies. Dashed lines represent the training sample, while filled histograms represent the predicted sample.

preserve the overall characteristics of the training data, ensuring that the classifier does not introduce significant biases in terms of redshift, morphology, stellar mass, gas content, or colors. By examining these distributions,

we can confirm that the predicted samples remain consistent with the physical trends observed in the training set, providing confidence that the classifier produces physically meaningful results across the full galaxy sample.

## REFERENCES

- Abazajian, K. N., Adelman-McCarthy, J. K., Agüeros, M. A., et al. 2009, *ApJS*, 182, 543, doi: [10.1088/0067-0049/182/2/543](https://doi.org/10.1088/0067-0049/182/2/543)
- Aguado, D. S., Ahumada, R., Almeida, A., et al. 2019, *ApJS*, 240, 23, doi: [10.3847/1538-4365/aaf651](https://doi.org/10.3847/1538-4365/aaf651)
- Akiba, T., Sano, S., Yanase, T., Ohta, T., & Koyama, M. 2019, arXiv e-prints, arXiv:1907.10902, doi: [10.48550/arXiv.1907.10902](https://doi.org/10.48550/arXiv.1907.10902)
- Ann, H. B., & Park, J.-C. 2006, *New Astronomy*, 11, 293
- Binney, J. 1992, *ARA&A*, 30, 51, doi: [10.1146/annurev.aa.30.090192.000411](https://doi.org/10.1146/annurev.aa.30.090192.000411)
- . 2024, *MNRAS*, 535, 1898, doi: [10.1093/mnras/stae2481](https://doi.org/10.1093/mnras/stae2481)
- Bluck, A. F. L., Mendel, J. T., Ellison, S. L., et al. 2014, *MNRAS*, 441, 599, doi: [10.1093/mnras/stu594](https://doi.org/10.1093/mnras/stu594)
- Briggs, F. H. 1990, *ApJ*, 352, 15, doi: [10.1086/168512](https://doi.org/10.1086/168512)
- Burke, B. F. 1957, *AJ*, 62, 90, doi: [10.1086/107463](https://doi.org/10.1086/107463)
- Debattista, V. P., & Sellwood, J. A. 1999, *ApJL*, 513, L107, doi: [10.1086/311913](https://doi.org/10.1086/311913)
- Dey, A., Schlegel, D. J., Lang, D., et al. 2019, *The Astronomical Journal*, 157, 168, doi: [10.3847/1538-3881/ab089d](https://doi.org/10.3847/1538-3881/ab089d)
- Djorgovski, S., & Sosin, C. 1989, *ApJL*, 341, L13, doi: [10.1086/185446](https://doi.org/10.1086/185446)
- Flaugher, B., Diehl, H. T., Honscheid, K., et al. 2015, *The Astronomical Journal*, 150, 150, doi: [10.1088/0004-6256/150/5/150](https://doi.org/10.1088/0004-6256/150/5/150)
- García-Ruiz, I., Kuijken, K., & Dubinski, J. 2002, *MNRAS*, 337, 459, doi: [10.1046/j.1365-8711.2002.05923.x](https://doi.org/10.1046/j.1365-8711.2002.05923.x)
- Han, J. J., Conroy, C., & Hernquist, L. 2023a, *Nature Astronomy*, 7, 1481, doi: [10.1038/s41550-023-02076-9](https://doi.org/10.1038/s41550-023-02076-9)
- Han, J. J., Semenov, V., Conroy, C., & Hernquist, L. 2023b, *ApJL*, 957, L24, doi: [10.3847/2041-8213/ad0641](https://doi.org/10.3847/2041-8213/ad0641)
- Haynes, M. P., Giovanelli, R., Kent, B. R., et al. 2018, *ApJ*, 861, 49, doi: [10.3847/1538-4357/aac956](https://doi.org/10.3847/1538-4357/aac956)
- Hunt, J. A. S., & Vasiliev, E. 2025, *NewAR*, 100, 101721, doi: [10.1016/j.newar.2024.101721](https://doi.org/10.1016/j.newar.2024.101721)
- Ibata, R., Lewis, G. F., Irwin, M., Totten, E., & Quinn, T. 2001, *ApJ*, 551, 294, doi: [10.1086/320060](https://doi.org/10.1086/320060)
- Johnston, K. V., Zhao, H., Spergel, D. N., & Hernquist, L. 1999, *ApJL*, 512, L109, doi: [10.1086/311876](https://doi.org/10.1086/311876)
- Jónsson, V. H., & McMillan, P. J. 2024, *A&A*, 688, A38, doi: [10.1051/0004-6361/202449744](https://doi.org/10.1051/0004-6361/202449744)
- Kerr, F. J. 1957, *AJ*, 62, 93, doi: [10.1086/107466](https://doi.org/10.1086/107466)
- Kormendy, J., & Ho, L. C. 2013, *ARA&A*, 51, 511, doi: [10.1146/annurev-astro-082708-101811](https://doi.org/10.1146/annurev-astro-082708-101811)
- Kormendy, J., & Kennicutt, Jr., R. C. 2004, *ARA&A*, 42, 603, doi: [10.1146/annurev.astro.42.053102.134024](https://doi.org/10.1146/annurev.astro.42.053102.134024)
- Laporte, C. F. P., Johnston, K. V., Gómez, F. A., Garavito-Camargo, N., & Besla, G. 2018, *MNRAS*, 481, 286, doi: [10.1093/mnras/sty1574](https://doi.org/10.1093/mnras/sty1574)
- Nurhidayat, R. M., Arifyanto, M. I., & Puspitarini, L. 2020, in *European Physical Journal Web of Conferences*, Vol. 240, *European Physical Journal Web of Conferences*, 07008, doi: [10.1051/epjconf/202024007008](https://doi.org/10.1051/epjconf/202024007008)
- Reshetnikov, V., & Combes, F. 1998a, *A&A*, 337, 9, doi: [10.48550/arXiv.astro-ph/9806114](https://doi.org/10.48550/arXiv.astro-ph/9806114)
- . 1998b, *A&A*, 337, 9, doi: [10.48550/arXiv.astro-ph/9806114](https://doi.org/10.48550/arXiv.astro-ph/9806114)
- Reshetnikov, V. P. 1995, *Astronomical and Astrophysical Transactions*, 8, 31, doi: [10.1080/10556799508203294](https://doi.org/10.1080/10556799508203294)
- Reshetnikov, V. P., Chugunov, I. V., Marchuk, A. A., et al. 2025, *Galactic warps: from cosmic noon to the current epoch*, arXiv, doi: [10.48550/arXiv.2504.12403](https://doi.org/10.48550/arXiv.2504.12403)
- Roškar, R., Debattista, V. P., Brooks, A. M., et al. 2010, *MNRAS*, 408, 783, doi: [10.1111/j.1365-2966.2010.17178.x](https://doi.org/10.1111/j.1365-2966.2010.17178.x)
- Sakamoto, K., Okumura, S. K., Ishizuki, S., & Scoville, N. Z. 1999, *ApJ*, 525, 691, doi: [10.1086/307910](https://doi.org/10.1086/307910)
- Saroon, S., & Subramanian, S. 2022, *A&A*, 666, A103, doi: [10.1051/0004-6361/202141435](https://doi.org/10.1051/0004-6361/202141435)
- Sellwood, J. A. 1996, *ApJ*, 473, 733, doi: [10.1086/178185](https://doi.org/10.1086/178185)
- Sheth, K., Vogel, S. N., Regan, M. W., Thornley, M. D., & Teuben, P. J. 2005, *ApJ*, 632, 217, doi: [10.1086/432409](https://doi.org/10.1086/432409)
- Shlosman, I., Frank, J., & Begelman, M. C. 1989, *Nature*, 338, 45, doi: [10.1038/338045a0](https://doi.org/10.1038/338045a0)
- Skryabina, A., Reshetnikov, V., Sotnikova, N., et al. 2024, *Monthly Notices of the Royal Astronomical Society*
- Sparke, L. S., & Casertano, S. 1988, *MNRAS*, 234, 873, doi: [10.1093/mnras/234.4.873](https://doi.org/10.1093/mnras/234.4.873)
- Speagle, J. S., Steinhardt, C. L., Capak, P. L., & Silverman, J. D. 2014, *ApJS*, 214, 15, doi: [10.1088/0067-0049/214/2/15](https://doi.org/10.1088/0067-0049/214/2/15)
- Springel, V., & White, S. D. M. 1999, *MNRAS*, 307, 162, doi: [10.1046/j.1365-8711.1999.02613.x](https://doi.org/10.1046/j.1365-8711.1999.02613.x)

- Sánchez-Saavedra, M. L., Battaner, E., & Guijarro, A. 2003, *Astronomy & Astrophysics*, 399, 457
- Tan, M., & Le, Q. V. 2019, in *Proceedings of Machine Learning Research*, Vol. 97, *Proceedings of the 36th International Conference on Machine Learning (PMLR)*, 6105–6114.  
<https://proceedings.mlr.press/v97/tan19a.html>
- van de Voort, F., Davis, T. A., Kereš, D., et al. 2015, *MNRAS*, 451, 3269, doi: [10.1093/mnras/stv1217](https://doi.org/10.1093/mnras/stv1217)
- Walmsley, M., Lintott, C., Géron, T., et al. 2021, *Monthly Notices of the Royal Astronomical Society*, 509, 3966, doi: [10.1093/mnras/stab2093](https://doi.org/10.1093/mnras/stab2093)
- Walmsley, M., Géron, T., Kruk, S., et al. 2023, *Monthly Notices of the Royal Astronomical Society*, 526, 4768, doi: [10.1093/mnras/stad2919](https://doi.org/10.1093/mnras/stad2919)
- Weinberg, M. D. 1998, *MNRAS*, 299, 499, doi: [10.1046/j.1365-8711.1998.01790.x](https://doi.org/10.1046/j.1365-8711.1998.01790.x)
- Yang, X., Mo, H. J., van den Bosch, F. C., et al. 2007, *ApJ*, 671, 153, doi: [10.1086/522027](https://doi.org/10.1086/522027)
- Zhou, R., Newman, J. A., Mao, Y.-Y., et al. 2021, *MNRAS*, 501, 3309, doi: [10.1093/mnras/staa3764](https://doi.org/10.1093/mnras/staa3764)